



Cite this: *J. Mater. Chem. C*, 2022, 10, 14194

## P25-induced polydopamine conformal assembly on Cu<sub>2</sub>O polyhedra for hydrophilic and stable photoelectrochemical performance

Lilai Sun,<sup>a</sup> Lu Han,<sup>a</sup> \*<sup>a</sup> Na Li,<sup>a</sup> Pengbo Wang,<sup>a</sup> Mingyue Wang,<sup>a</sup> Xudong Luo<sup>a</sup> and Xibao Li \*<sup>b</sup>

Cu<sub>2</sub>O has begun to show its charm and gain popularity in various photoelectrochemical (PEC) processes, but fast charge recombination and photochemical instability always limit its PEC water splitting activity and stability. Furthermore, H<sub>2</sub>O wetting on the Cu<sub>2</sub>O photocathode is the premise for PEC reaction, while research on carrier separation, photostability and still wettability has not been brought to the forefront. Herein, a self-polymerized dopamine coating is employed to directly anchor TiO<sub>2</sub> (P25) on the surface of a Cu<sub>2</sub>O film electrode; nanoscale particles facilitate polydopamine (PDA) conformal assembly on Cu<sub>2</sub>O polyhedra. A ternary Cu<sub>2</sub>O/PDA/TiO<sub>2</sub> composite photocathode is obtained and shows boosted PEC activity and stability. The advantages of this unique design are mainly reflected in three aspects: (1) the married heterojunction of TiO<sub>2</sub>/Cu<sub>2</sub>O provides a persistent driving force for charge separation by PDA natural adhesive properties; (2) the conversion of hydrophobicity–hydrophilicity is achieved to improve the wettability of the Cu<sub>2</sub>O film electrode assisted by conformal PDA coating; (3) the improvement of PEC stability is due to the inhibition of Cu<sub>2</sub>O photocorrosion covered by the PDA shelter. This advance bodes well for the development of the PEC field founded on multifunctional PDA.

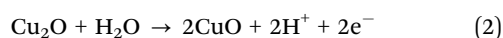
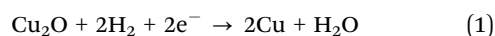
Received 25th July 2022,  
Accepted 30th August 2022

DOI: 10.1039/d2tc03116g

rsc.li/materials-c

## Introduction

Photocatalysis and photoelectrocatalysis have attracted a lot of attention as an environmentally friendly technology.<sup>1–5</sup> Cuprous oxide has attracted great attention in the field of photocatalysis and photoelectrocatalysis due to its narrow band gap (~2.0 eV), which is capable of absorbing visible light that maximizes sunlight harvesting.<sup>6–8</sup> Photochemistry stable Cu<sub>2</sub>O is the premise to perform catalytic processes. However, the practical application of the Cu<sub>2</sub>O photocathode is still limited by the fact that it suffers from detrimental photocorrosion. The transformations of Cu<sub>2</sub>O to CuO and Cu are unavoidable (eqn (1) and (2)) because of its self-oxidation and self-reduction.<sup>9</sup> Moreover, photogenerated carrier recombination often exists for most semiconductors under irradiation, which deeply affects the utilization of carriers and negatively drives redox reactions.



TiO<sub>2</sub> plays a positive role in alleviating the above photocorrosion and carrier recombination. By knowing the dominant deactivation mode of Cu<sub>2</sub>O, fabricating a chemically inert coating is an effective way to prevent Cu<sub>2</sub>O from contacting the electrolyte solution with redox activity.<sup>10,11</sup> A TiO<sub>2</sub> coating is an excellent candidate, which allows photogenerated electrons to transfer through owing to its appropriate conduction band position.<sup>12,13</sup> An atomic layer deposited TiO<sub>2</sub> coating can efficiently improve the stability of the p–n Cu<sub>2</sub>O photocathode in aqueous conditions reported by Gong *et al.*<sup>14</sup> Furthermore, lowering the diffusion energy barrier of photogenerated carriers can be achieved by constructing a semiconductor heterojunction. The formed type-II or direct Z heterojunction by TiO<sub>2</sub>/Cu<sub>2</sub>O provides a strong driving force for charge separation.<sup>15,16</sup> Zhang *et al.*<sup>17</sup> reported that the Cu<sub>2</sub>O/TiO<sub>2</sub> p–n heterojunction exhibited better H<sub>2</sub> production activity and stability than pure Cu<sub>2</sub>O and TiO<sub>2</sub>.

In addition, the PEC process and performance is deeply affected kinetically by the adsorption and desorption of reactants and products.<sup>18</sup> Theoretically, proper wettability can promote the adsorption of reactants.<sup>19</sup> H<sub>2</sub>O attached to the photocathode serves as a reactant in PEC water splitting. In this case, the hydrophilicity of the Cu<sub>2</sub>O photocathode is particularly important. Zhao *et al.*<sup>20</sup> electrodeposited NiFe hydroxide/NiFe phosphate on carbon fiber paper. The phosphate groups improved the

<sup>a</sup> School of Materials and Metallurgy, University of Science and Technology Liaoning, Anshan, 114051, China. E-mail: hanlu@ustl.edu.cn

<sup>b</sup> School of Materials Science and Engineering, Nanchang Hangkong University, Nanchang, 330063, China. E-mail: lixibao@nchu.edu.cn

electrode surface wettability and created more accessible active sites, which meant that electrons could transfer rapidly. Wang *et al.*<sup>21</sup> modified a variety of molecular monolayers with different functional groups on TiO<sub>2</sub> nanotube arrays. The surface chemical composition and wettability of the photoelectrode influenced the oxidation–reduction reaction on the surface and interface. Takayuki *et al.*<sup>22</sup> observed that the bubble size on the electrode surface increased with the decrease of the wettability through an *in situ* video during the HER. This result means that ohmic loss was increased and the electrode active surface was blocked. These reports indicate that the wettability of the electrode surface has an important effect on catalytic activity. However, efforts to improve the Cu<sub>2</sub>O photocathode wettability for PEC water splitting have not been brought to the forefront. Almost no work takes into account photostability, carrier separation and still wettability for the Cu<sub>2</sub>O photocathode.

Herein, we report a simple nanoscale TiO<sub>2</sub>-induced polymerization of biology-based dopamine on a Cu<sub>2</sub>O polyhedron photocathode to enhance the PEC activity and stability. This work creatively introduces functional nanoparticles to optimize dopamine polymerization on an uneven and hydrophobic Cu<sub>2</sub>O polyhedron photocathode, not only fabricating a novel and married Cu<sub>2</sub>O/PDA/TiO<sub>2</sub> heterojunction structure and creating a hydrophilic reduction reaction interface by the buried nanoparticle PDA overlayer for highly efficient PEC H<sub>2</sub>O reduction, but also providing a novel strategy for improving the photochemical stability of Cu<sub>2</sub>O semiconductors in various applications.

## Experimental

### Materials

Copper sulfate pentahydrate (CuSO<sub>4</sub>·5H<sub>2</sub>O), sodium hydroxide (NaOH), lactic acid (C<sub>3</sub>H<sub>6</sub>O<sub>3</sub>, 80%), dopamine hydrochloride and tris(hydroxymethyl)aminomethane were purchased from Aladdin (China). Titanium dioxide (TiO<sub>2</sub>, P25) was purchased from Sigma (USA). All chemicals were used as received without further treatment.

### Preparation of photocathodes

The pristine Cu<sub>2</sub>O electrodes were prepared by the electrodeposition method. In a typical experiment, an FTO substrate (20 × 10 × 1.6 mm, 14 Ω) was cleaned in acetone, ethanol and deionized (DI) water with sonication, sequentially. The electrodeposition of Cu<sub>2</sub>O was performed using an IviumStat electrochemical workstation with a three-electrode configuration, in which the FTO substrate served as the working electrode, a platinum plate as the counter electrode and the Ag/AgCl electrode as the reference electrode, respectively. The deposition was conducted at a potential difference of −0.4 V in an electrolyte solution consisting of 0.4 M CuSO<sub>4</sub> and 3 M lactic acid. The pH of the electrolyte solution was adjusted to 11.5 by the addition of 5 M NaOH solution. Cu<sub>2</sub>O thin films were prepared by electrodeposition while the temperature was kept at 60 °C using a hot water bath with a temperature probe.

Cu<sub>2</sub>O/PDA electrodes were prepared by self-polymerization of dopamine. First, 0.1 g dopamine hydrochloride was fully dissolved in an appropriate amount of tris–HCl buffer (pH = 8.6, 2 mM) to form a dopamine solution with a concentration of 2 mg mL<sup>−1</sup>. Then, the Cu<sub>2</sub>O electrode was immersed in the above solution, and a PDA coating was polymerized on the electrode surface after 3 h.

The preparation method of the Cu<sub>2</sub>O/PDA/P25 electrode was similar to the previous method, but an additional 0.1 g P25 was added to the solution.

For comparison, Cu<sub>2</sub>O/P25 electrodes were prepared just by immersing Cu<sub>2</sub>O electrodes in the solution by dissolving 0.1 g of P25 in 50 mL of DI water.

### Characterization techniques

The crystal structures of the prepared samples were obtained by X-ray diffractometer with Cu Kα radiation (X' Pert Powder, PANalytical B.V.). A Zeiss-ΣIGMA field emission scanning electron microscope (FESEM, Germany) was used to characterize the morphology of the prepared samples at 10 kV acceleration voltage. Atomic force microscopy (AFM) measurements were performed on a Dimension Icon (Bruker) using tapping mode. The chemical state and elemental compositions were recorded by X-ray photoelectron spectroscopy (XPS) with a monochromatic Al Kα source at 12 kV operating voltage (Thermo Scientific K-Alpha, UK). The water contact angles of the as-fabricated electrode thin films were obtained at ambient temperature conditions utilizing a standard goniometer (JY-82B Kruss DSA, Germany). UV-vis diffuse reflectance spectra (UV-vis DRS) were measured on a spectrophotometer (Shimadzu UV-3600, Japan) in the range of 300–800 nm. Photoluminescence (PL) spectra were obtained by a spectrophotometer (Edinburgh FLS1000, UK) with an excitation wavelength of 255 nm at room temperature.

### Photoelectrochemical tests

In this study, all photoelectrochemical performance measurements were completed on the CHI760E electrochemical workstation (Chenhua, Shanghai). The traditional three electrodes were composed of 0.1 M Na<sub>2</sub>SO<sub>4</sub> aqueous solutions. The prepared samples were used as working electrodes, Pt plate as a counter electrode, and Ag/AgCl in saturated KCl as a reference electrode. A 300 W Xenon lamp with the intensity of 100 mW cm<sup>−2</sup> (similar to an AM 1.5 sun illumination) was used as the light source (PLS-SXE300, Beijing Perfectlight). For all the samples, a scan rate of 10 mV s<sup>−1</sup> was used for the linear sweep voltammetry measurements in the test range of 0 to 0.6 V. Amperometric *I*–*t* curves were obtained by illuminating and avoiding light under the bias voltage of 0 V.

Electrochemical impedance spectroscopy (EIS) was performed using an AC amplitude of 5 mV and a frequency range between 100 kHz and 1 Hz. The measured EIS data were obtained at an open circuit voltage under illumination. All of the potentials mentioned above were converted to the RHE reference electrode by the Nernst equation:

$$E_{\text{RHE}}(\text{V}) = E_{\text{Ag/AgCl}}(\text{V}) + 0.059 \text{ pH} + 0.197$$

The applied bias photon-to-current efficiency (ABPE) was calculated as follows:

$$\text{ABPE} = \frac{V_{\text{RHE}} \times |I_{\text{light}}|}{P} \times 100\%$$

where  $I_{\text{light}}$  and  $P$  are the photocurrent density and intensity of the incident light, respectively.

In Mott–Schottky measurements, potential sweeps were carried out from 0.5 V to  $-0.7$  V vs. Ag/AgCl. The AC frequency used in the impedance measurements was 50 Hz. The calculation of valence band and carrier concentration is based on previous work.<sup>23</sup>

### Time-resolved photoluminescence

The data are fitted using a biexponential decay model,  $y = B_1 \exp\left(-\frac{t}{\tau_1}\right) + B_2 \exp\left(-\frac{t}{\tau_2}\right)$ , from which an intensity-averaged carrier lifetime  $\tau_{\text{av}}$  is computed to compare charge transfer dynamics.  $\tau_{\text{av}}$  can be estimated as

$$\tau_{\text{av}} = \frac{B_1 \tau_1^2 + B_2 \tau_2^2}{B_1 \tau_1 + B_2 \tau_2}$$

$k_{\text{ct}}$  is the charge transfer rate constant.  $k_{\text{ct}}$  can be estimated as

$$k_{\text{ct}} = \frac{1}{\tau_{\text{av}}}(\text{composite}) - \frac{1}{\tau_{\text{av}}}(\text{purity})$$

## Results and discussion

Fig. 1 records XRD patterns of four electrodes and P25 nanoparticles. The peaks at  $36.5^\circ$  and  $60.4^\circ$  are ascribed to the (111) and (220) crystal planes of  $\text{Cu}_2\text{O}$  crystals. A weak peak belonging to the anatase (101) crystal plane appears at  $25.3^\circ$ , indicating the presence of P25 nanoparticles in  $\text{Cu}_2\text{O}/\text{PDA}/\text{P25}$  and  $\text{Cu}_2\text{O}/\text{P25}$ . The XRD pattern of PDA is absent due to the amorphous nature of the polymer.<sup>24</sup>



Fig. 1 XRD patterns of different electrodes and P25 particles.

XPS analysis was conducted to confirm the surface chemical state details. Fig. 2(a) exhibits the survey spectrum, where Cu 2p, C 1s and O 1s signals are clearly observed in the obtained samples. Fig. 2(b) and (d) show typical N 1s spectra of  $\text{Cu}_2\text{O}/\text{PDA}$  and  $\text{Cu}_2\text{O}/\text{PDA}/\text{P25}$ . The high-resolution N 1s region is fit with three peaks assigned to primary ( $\text{R-NH}_2$ ), secondary ( $\text{R-NH-R}$ ), and tertiary/aromatic ( $=\text{N-R}$ ) amine functionalities, which represent the chemical bonds of polydopamine and its intermediates, respectively.<sup>25–27</sup> The two characteristic peaks of 951.72 eV and 931.93 eV in the high-resolution XPS spectrum of Cu 2p (Fig. 2(b)) correspond to Cu 2p<sub>1/2</sub> and Cu 2p<sub>3/2</sub>, respectively, which are consistent with the characteristics of  $\text{Cu}^+$  in  $\text{Cu}_2\text{O}$ .<sup>28</sup> The remaining two peaks at 946.37 and 943.37 eV are satellite peaks of  $\text{Cu}^+$ .<sup>29</sup> The signal of N 1s and Ti 2p peaks can be clearly observed in  $\text{Cu}_2\text{O}/\text{PDA}/\text{P25}$ , whereas the signal of the Cu 2p peak became weak after the introduction of PDA, which demonstrated that the PDA coating can act as a shield, affecting the X-ray diffraction toward the  $\text{Cu}_2\text{O}$ . Two characteristic peaks in the high-resolution spectrum of Ti 2p at 464.08 eV and 458.38 eV shown in Fig. 2(d) also correspond to 2p<sub>1/2</sub> and 2p<sub>3/2</sub>, and the other peak is a satellite peak. All of the results indicated the successful encapsulation of P25 nanoparticles into a PDA coating on  $\text{Cu}_2\text{O}$  substances.

The surface morphology and wettability of the electrodes were analyzed using AFM and the contact angle underwater, as shown in Fig. 3(a)–(d). The measured roughness values ( $R_a$ ) are 122 nm, 119 nm, 143 nm and 98 nm, respectively. The uniformly

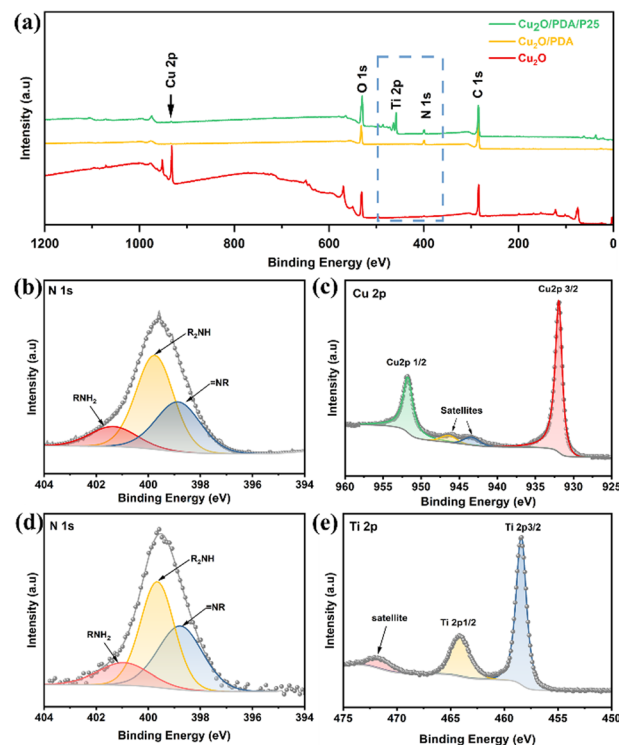


Fig. 2 (a) XPS pattern full spectra of  $\text{Cu}_2\text{O}$ ,  $\text{Cu}_2\text{O}/\text{PDA}$  and  $\text{Cu}_2\text{O}/\text{PDA}/\text{P25}$ . (b) High-resolution XPS spectra of N 1s in  $\text{Cu}_2\text{O}/\text{PDA}$  and (c) Cu 2p in  $\text{Cu}_2\text{O}$ . (d) High-resolution XPS spectra of N 1s in  $\text{Cu}_2\text{O}/\text{PDA}/\text{P25}$  and (e) Ti 2p.

smooth cubic and pyramidal grains of  $\text{Cu}_2\text{O}$  can be observed on the AFM 3D images and SEM image of the  $\text{Cu}_2\text{O}$  electrode. The morphology of  $\text{Cu}_2\text{O}$  is similar to that reported previously (Fig. 3(e)).<sup>30</sup> The pristine  $\text{Cu}_2\text{O}$  electrode's contact angle is  $92.96^\circ$ , showing its hydrophobicity (Fig. 3(a)). Self-polymerization of dopamine onto the  $\text{Cu}_2\text{O}$  polyhedron electrode surface forms a coating with nanoscale thickness, as shown in Fig. 3(b) and (f); meanwhile the contact angle becomes significantly smaller at  $77.12^\circ$ , which is due to the successful anchoring of numerous hydrophilic groups arising from the PDA coating.<sup>31</sup> PDA-induced surface modification is again echoed in the XPS results. It is believed that the transition from hydrophobicity to hydrophilicity may accelerate the reaction dynamics of water participation, resulting in improvement of the PEC activity. After introducing hydrophobic P25 nanoparticles, the contact angle becomes larger at  $120.59^\circ$ . As is shown in Fig. 3(c), P25 nanoparticles tend to

cluster in the protruding part of the  $\text{Cu}_2\text{O}$  pyramidal grains, resulting in a greater surface roughness. According to the Wenzel model, the greater the roughness on the hydrophobic surface, the more hydrophobic it is.<sup>32,33</sup> Interestingly, the surface hydrophobicity reverses when P25 nanoparticles are used in combination with dopamine. On the one hand, the nanoparticles speed up the polymerization of dopamine.<sup>34,35</sup> On the other hand, they would be drawn into the viscous fluid to fill the gaps of the uneven  $\text{Cu}_2\text{O}$  pyramidal grains, reducing the surface roughness of the electrode. Nanoscale particles better collaborate surface hydrophilic modification,<sup>36</sup> resulting in a smaller roughness of the  $\text{Cu}_2\text{O}$  pyramidal grains, presenting hydrophilicity with a smaller contact angle of  $64.79^\circ$  on the electrode surface (Fig. 3(d) and (g)). And the membrane of  $3.3 \mu\text{m}$  thickness was observed through the side image of SEM (Fig. 3(h)). An enhanced interface hydrophilicity was achieved by polymerizing dopamine assisted by P25 onto the surface of the  $\text{Cu}_2\text{O}/\text{TiO}_2$  heterostructure. The novel integration of inorganic and organic materials would create a synergistic modification effect for the unstable and hydrophobic  $\text{Cu}_2\text{O}$  photocathode to yield enhanced PEC water reduction performance.

Linear sweep voltammetry (LSV) curves record the photocurrent response impacted by applied potential, as shown in Fig. 4(a). Pristine  $\text{Cu}_2\text{O}$  exhibits  $1 \text{ mA cm}^{-2}$  photoresponse at  $0 \text{ V vs. RHE}$  due to the presence of surface recombination sites of bare  $\text{Cu}_2\text{O}$  in practical applications; besides, the photocurrent density of either  $\text{Cu}_2\text{O}/\text{PDA}$  or  $\text{Cu}_2\text{O}/\text{P25}$  increased remarkably, indicating that hydrophilic modification, photosensitivity and the p/n heterojunction are conducive to the carrier separation and transfer.<sup>17,22</sup> In particular, at  $0 \text{ V vs. RHE}$ , the photocurrent in  $\text{Cu}_2\text{O}/\text{PDA}/\text{P25}$  yields  $2.3 \text{ mA cm}^{-2}$ , which is approximately 2.3 times that of the pristine  $\text{Cu}_2\text{O}$  electrode. Accordingly, the applied bias photon-to-current efficiency (ABPE) reaches up to 0.12%, which is about 4 times higher than that of the  $\text{Cu}_2\text{O}$  electrode (Fig. 4(b)).

Amperometric  $I-t$  curves are presented in Fig. 4(c), showing a renewable and fast photocurrent response. The photocurrent density remains uniform with the LSV curves above mentioned.

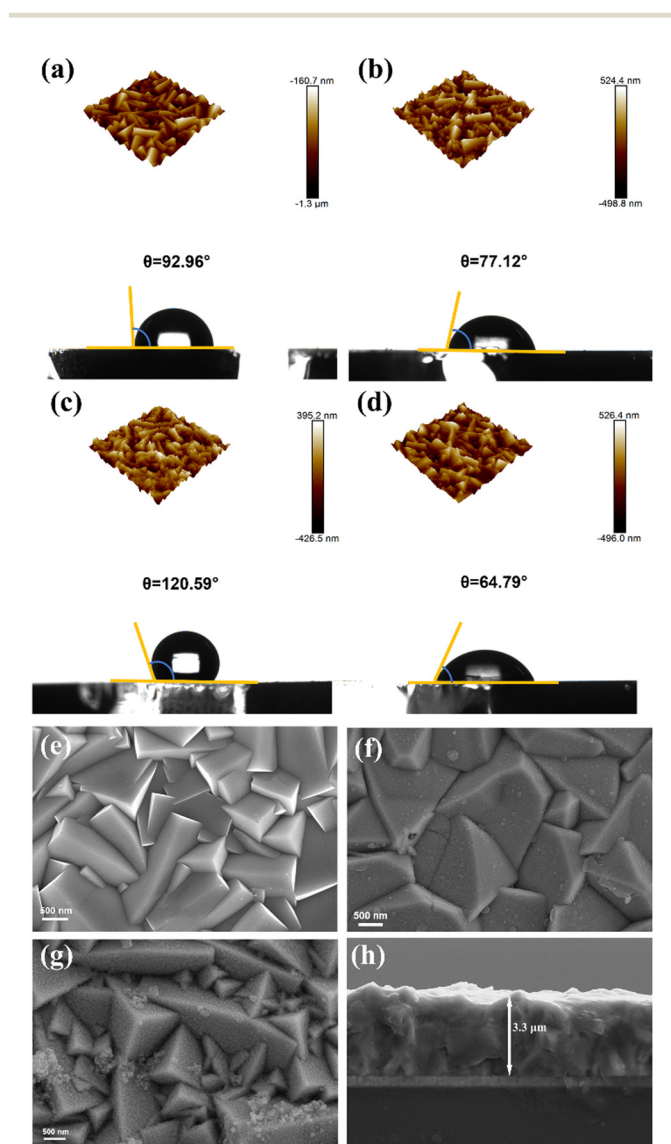


Fig. 3 AFM 3D image of a  $10 \times 10 \mu\text{m}^2$  region and their contact angle of (a)  $\text{Cu}_2\text{O}$ , (b)  $\text{Cu}_2\text{O}/\text{PDA}$ , (c)  $\text{Cu}_2\text{O}/\text{P25}$  and (d)  $\text{Cu}_2\text{O}/\text{PDA}/\text{P25}$ . SEM image of (e)  $\text{Cu}_2\text{O}$ , (f)  $\text{Cu}_2\text{O}/\text{PDA}$ , (g)  $\text{Cu}_2\text{O}/\text{PDA}/\text{P25}$  and its side image (h).

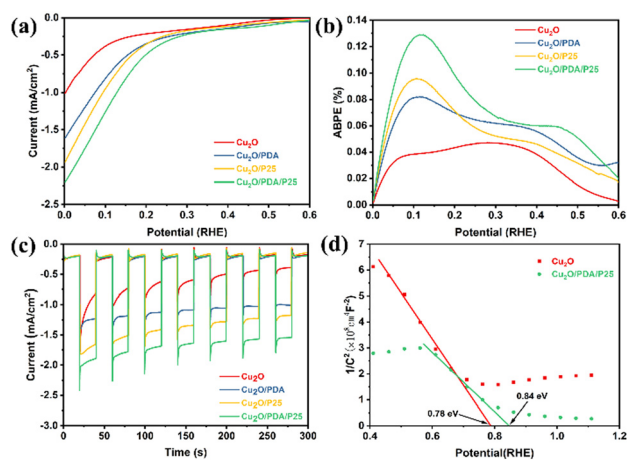


Fig. 4 (a) Linear sweep voltammetry curves. (b) ABPE. (c) Amperometric  $I-t$  curves. (d) Mott-Schottky test.



It can be noticed that the photocurrent density of the pristine  $\text{Cu}_2\text{O}$  electrode declines rapidly with test time, implying its instability under irradiation in electrolyte. A sluggish descent of photocurrent is observed when introducing a PDA overlayer, implying that photocorrosion is obviously alleviated. This improvement is more effective and persistent as the PDA layer provides shelter for  $\text{Cu}_2\text{O}$ , delaying the loss resulting from photooxidation and photoreduction of  $\text{Cu}_2\text{O}$ , but is not thick enough to have a light-shielding effect to weaken electronic migration. Nevertheless the PDA after polymerization within a short time has tiny pinholes,<sup>37</sup> so a sluggish photocorrosion over  $\text{Cu}_2\text{O}/\text{PDA}$  may still proceed with constant light. Besides, the formation of the  $\text{Cu}_2\text{O}/\text{P25}$  heterojunction promotes the transfer of photogenerated carriers, which inhibits the photocorrosion of  $\text{Cu}_2\text{O}$  to a certain extent. On the integration of PDA and P25, a synchronous promotion of photocurrent density and stability was obtained. As for the improved photocurrent density, naturally viscous PDA induced married heterogeneous junctions between  $\text{Cu}_2\text{O}$  and commercial P25 to further promote carrier separation.<sup>38</sup> In addition, modifying the  $\text{Cu}_2\text{O}$  photocathode hydrophobicity by decorating with a PDA coating buried P25 to improve its hydrophilicity is achieved, enhancing the adsorption of the reactants ( $\text{H}^+/\text{H}_2\text{O}$ ). A Mott–Schottky test was performed on the electrodes, as shown in Fig. 4(d). The slope of the linear part of the curve is negative, which also proves that the  $\text{Cu}_2\text{O}$  conductivity type on the electrodeposition was p-type.<sup>39</sup> The flat-band potentials of  $\text{Cu}_2\text{O}$  and  $\text{Cu}_2\text{O}/\text{PDA}/\text{P25}$  are 0.78 eV and 0.83 eV, and the carrier densities are  $1.036 \times 10^{-21} \text{ cm}^{-3}$  and  $1.61 \times 10^{-21} \text{ cm}^{-3}$ , respectively. Thus, this kinetically facilitates the reaction from promoting the carrier separation and transfer and thus the photocurrent density becomes larger. Echoing the results of Fig. 3(d), the best stability in the photocathode half reaction is on account of the markedly improved photocorrosion resistance of  $\text{Cu}_2\text{O}$ , resulting from the unique space-filling P25 induced PDA overlayer.

According to the above experimental results, the enhanced PEC activities are attributed to the unique structure composed of space-filling P25 induced PDA overlayer. To further prove this assumption, the photoexcitation process was studied by photoluminescence (PL) spectra to probe the internal electron transfer dynamics.<sup>40</sup> As shown in Fig. 5(a), all four electrodes have two distinct emission bands, which are mainly attributed

to the band gap emission and the radiative transition due to the defect state.<sup>41</sup> The peak nearly at 470 nm is attributed to the band gap emission. And another emission band centered at 680–710 nm is the radiative transition due to the defect state. The luminescence intensity of the  $\text{Cu}_2\text{O}/\text{PDA}/\text{P25}$  composite electrode decreases sharply compared to the other samples, which shows an efficient separation of the surface electron–hole pairs and a significant suppression of the photogenerated carrier recombination. It's worth noting that the defect state emission becomes smaller after loading the PDA overlayer, which is proof of the passivation effect arising from PDA effectively reducing the electrode surface defects.<sup>24</sup>

Time resolved photoluminescence (TRPL) spectra were thereafter recorded and are displayed in Fig. 5(b), providing a quantitative lifetime of the photogenerated carrier.  $\tau_1$  and  $\tau_2$  represent the radiative and non-radiative recombination, respectively, and these two factors determine the electron dynamics.<sup>38,42</sup>  $\text{Cu}_2\text{O}/\text{PDA}/\text{P25}$  possesses the shortest  $\tau_1$  lifetime (0.24 ns) compared to  $\text{Cu}_2\text{O}$  (0.46 ns),  $\text{Cu}_2\text{O}/\text{PDA}$  (0.28 ns) and  $\text{Cu}_2\text{O}/\text{P25}$  (0.26 ns), which indicates its improved band-to-band recombination of charge carriers.<sup>43</sup> Meanwhile,  $\text{Cu}_2\text{O}/\text{PDA}/\text{P25}$  also owns the most efficient non-radiative decay pathway, giving the shortest  $\tau_2$  lifetime (2.09 ns).<sup>44</sup> The shortening of the average lifetime ( $\tau_{\text{av}}$ ) of  $\text{Cu}_2\text{O}/\text{PDA}/\text{P25}$  implies that integration of PDA and P25 allows efficient electron–hole separation and migration. Due to the synergistic effect of the married  $\text{Cu}_2\text{O}/\text{P25}$  heterojunction glued by PDA, surface passivation and increased wettability, the  $\text{Cu}_2\text{O}/\text{PDA}/\text{P25}$  ternary composite electrode possesses the largest transfer rate of photogenerated charge carriers.<sup>45</sup> The charge transfer rate constants ( $k_{\text{ct}}$ ) of  $\text{Cu}_2\text{O}/\text{PDA}$ ,  $\text{Cu}_2\text{O}/\text{P25}$  and  $\text{Cu}_2\text{O}/\text{PDA}/\text{P25}$  are calculated to be  $0.57 \times 10^9 \text{ s}^{-1}$ ,  $0.60 \times 10^9 \text{ s}^{-1}$  and  $1.87 \times 10^9 \text{ s}^{-1}$ , respectively. These quantified results provide strong evidence for the efficient charge transfer of the  $\text{Cu}_2\text{O}/\text{PDA}/\text{P25}$  electrode.<sup>46</sup> In addition, the electrochemical impedance spectroscopy (EIS) Nyquist spectrum is shown in Fig. 5(c). The smaller arc and smaller  $R_{\text{ct}}$  values indicate the smaller the charge transfer resistance between the electrode and electrolyte.<sup>47,48</sup> The wetter  $\text{Cu}_2\text{O}/\text{PDA}/\text{P25}$  electrode has a significantly lower surface charge transfer resistance. These charge dynamics results well match with the results of PEC performance. More efficient separation of photogenerated carriers and faster interfacial charge transfer favor higher PEC performance.<sup>49</sup> The rational design of an efficient carrier separation transfer path is

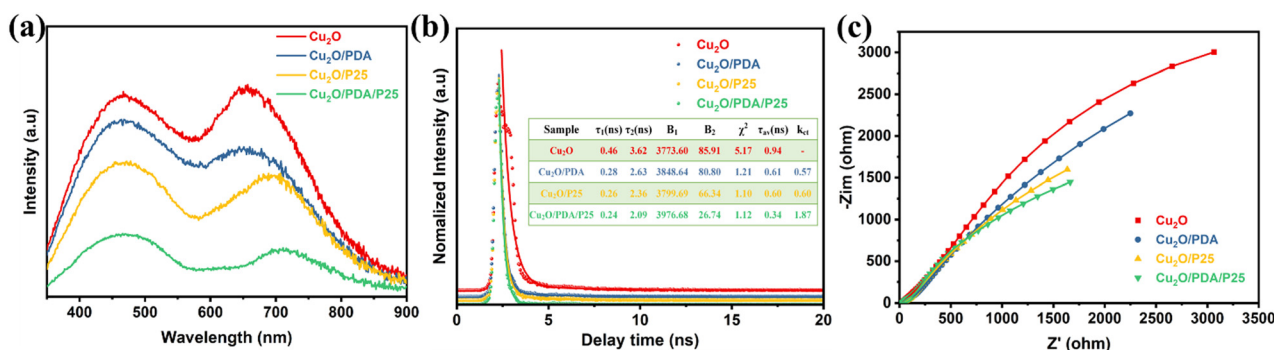


Fig. 5 (a) Room temperature PL spectra. (b) Fitted results of TRPL spectra. (c) Nyquist plots at open-circuit voltage under illumination.

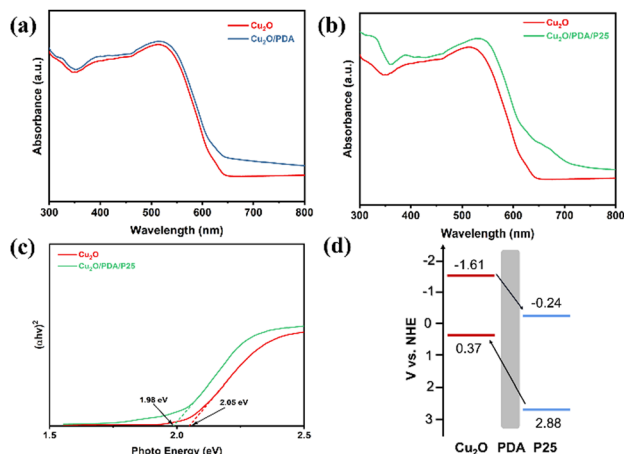


Fig. 6 The UV-vis diffuse reflectance spectra of (a)  $\text{Cu}_2\text{O}$  and  $\text{Cu}_2\text{O}/\text{PDA}$  and (b)  $\text{Cu}_2\text{O}$  and  $\text{Cu}_2\text{O}/\text{PDA}/\text{P25}$ , (c) Tauc plots, and (d) schematic diagram of charge transfer between  $\text{Cu}_2\text{O}$  and P25.

demonstrated by the PL and EIS results to achieve a lower carrier recombination rate.

The UV-Vis diffuse reflectance spectra are shown in Fig. 6(a) and (b). Compared with the  $\text{Cu}_2\text{O}$  electrode, PDA coating does not block light absorption because it is the eumelanin polymer that has high light absorption.<sup>50</sup> According to our previous work, the black PDA exhibits a good capability for light absorption between 200 and 800 nm.<sup>27</sup> Moreover, an apparent enhancement of absorption can be seen for the composites.<sup>51</sup> The band gap values of different electrodes are obtained from the Tauc plots, as shown in Fig. 6(c). From the calculated valence band and conduction band energy, a band diagram is presented in Fig. 6(d).<sup>52–54</sup>

On the basis of the analysis above, potential mechanisms of ternary  $\text{Cu}_2\text{O}/\text{PDA}/\text{P25}$  for PEC enhancement in activity and

stability have been further illustrated in Fig. 7. Under light illumination, the water reduction process based on the pristine  $\text{Cu}_2\text{O}$  polyhedron electrode gets a slow reaction kinetics, owing to its fast carrier recombination and surface hydrophobicity. Meanwhile, bare  $\text{Cu}_2\text{O}$  polyhedrons in direct contact with the electrolyte are also threatened by photocorrosion. Once the integration of inorganic P25 and organic dopamine is employed to modify the  $\text{Cu}_2\text{O}$  polyhedron surface, P25 nanoparticles as connectors are not only involved in accelerating the polymerization of dopamine but also they would be drawn into the viscous fluid to fill the gaps of the uneven  $\text{Cu}_2\text{O}$  pyramidal grains, forming a unique space-filling P25-induced PDA overlayer on  $\text{Cu}_2\text{O}$ . This is verified by both AFM images and contact angle analysis. The novel heterojunction structure set several favorable stages for PEC enhancement in activity and stability. Firstly, with P25 joining, a II-type heterojunction of  $\text{Cu}_2\text{O}/\text{TiO}_2$  is formed. Under light illumination, both  $\text{Cu}_2\text{O}$  and  $\text{TiO}_2$  simultaneously produce photo-induced electron-hole pairs. The electron and hole transfers are reversed under internal electric field forces due to the different energy band positions; electrons are transferred from  $\text{Cu}_2\text{O}$  to P25 and holes are transferred from P25 to  $\text{Cu}_2\text{O}$ . With the boost of PDA, the married coupling interfaces of the  $\text{TiO}_2/\text{Cu}_2\text{O}$  heterojunction provide a persistent driving force for charge separation. As a result, a lower charge recombination rate is achieved as proven by the PL and EIS results. Secondly, as an electron donor, PDA can also contribute to light absorption, which echoes the results of UV-Vis diffuse reflectance spectra. In particular, it is worth mentioning that there is no light-shielding in the ultrathin PDA layer, whose electronic tunneling effect is not weakened in the meantime. Thirdly, the gullies of the  $\text{Cu}_2\text{O}$  polyhedron surface were filled up with nanoscale P25 assisted by dopamine polymerization, causing roughness reduction. Thus, an improved hydrophilic PDA overlayer with numerous hydrophilic groups was coated on the  $\text{Cu}_2\text{O}$  polyhedron surface to reverse its hydrophobic disadvantage. This operation improves the wettability of the electrode surface and absorbs more reactants ( $\text{H}^+/\text{H}_2\text{O}$ ), thus kinetically promoting the rate of catalytic reaction and improving the catalytic activity. Finally, the unique space-filling P25 induced PDA overlayer provides structurally optimal shelter to satisfy the inhibition of  $\text{Cu}_2\text{O}$  photocorrosion from active radicals dissolved in the electrolyte, rendering the improvement sustainable. This echoes the results and discussions of amperometric  $I-t$  curves. In conclusion, we have assembled the multiple effects of polydopamine (Table 1); the integration of P25 and PDA induces a synergistic modification effect for the poor

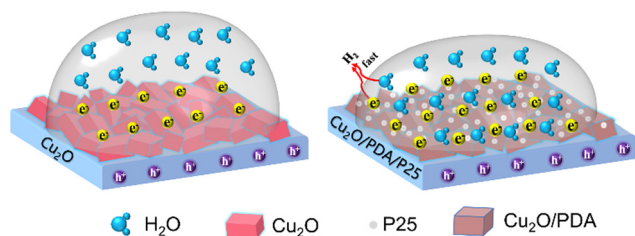


Fig. 7 The schematic of the catalytic reaction promoted by different wettability of the electrode surface.

Table 1 The functions of PDA in the field of PEC

Materials	Function	Ref.
$\text{Cu}_2\text{O}/\text{PDA}/\text{P25}$	Assisting in heterostructure construction, modulating wettability and inhibiting photocorrosion	This work
$\text{g-C}_3\text{N}_4/\text{PDA}/\text{BiOBr}$	PDA as an efficient electron transfer mediator	55
$\text{TiO}_2/\text{PDA}$	Enhancing the hole-electron separation and harvesting visible light	50
$\text{CdS}/\text{PDA}/\text{TiO}_2$ NTAs	Photosensitization and inhibition of CdS photocorrosion	27
$\text{Ti}/\text{TiO}_2\text{NT}/\text{PDA-AgNP}$	PDA coating can act as an <i>in situ</i> reducing agent capable of reducing some metal ions to form metal nanoparticles	56
$\text{PDA}_{15}/\text{ZnO}/\text{Co}_3\text{O}_4$	The enhanced $\text{CO}_2$ adsorption/activation capacity by PDA modification	57
$\text{Ag}/\text{AgCl}/\text{polydopamine TiO}_2$	The polydopamine acts as a stabilizer and reductant in fabricating the photocatalyst	58

carrier utilization, hydrophobic and unstable Cu<sub>2</sub>O photocathode to yield enhanced PEC water reduction performance.

## Conclusion

In summary, a self-polymerized dopamine coating is employed to directly anchor P25 on the surface of a Cu<sub>2</sub>O film electrode. And P25 particles are introduced creatively to facilitate PDA conformal assembly on Cu<sub>2</sub>O polyhedra. The hydrophilic PDA coating provides a reactant-rich concentration on the electrode surface to tip the reaction balance toward the synthesis of H<sub>2</sub>. The concept of forming a hydrophilic heterostructured Cu<sub>2</sub>O/PDA/P25 electrode enables advances in the high carrier utilization and high stability of Cu<sub>2</sub>O semiconductor PEC water reduction performance.

## Author contributions

L. Sun: experiments, data analysis, and writing – original draft. L. Han and X. Li: ideas, writing – review & editing, and funding acquisition. N. Li, P. Wang and M. Wang: helped with experiments and data analysis. X. Luo: project administration.

## Conflicts of interest

There are no conflicts to declare.

## Acknowledgements

The authors acknowledge the financial support from the National Natural Science Foundation of China (Grant no. U1908227, 51962023) and the Natural Science Foundation of Jiangxi Province, China (Grant no. 20212BAB204045). The authors would like to thank the shiyanjia lab ([www.shiyanjia.com](http://www.shiyanjia.com)) for the XPS test and PL test.

## Notes and references

- X. Li, Q. Luo, L. Han, F. Deng, Y. Yang and F. Dong, *J. Mater. Sci. Technol.*, 2022, **114**, 222–232.
- X. Li, B. Kang, F. Dong, Z. Zhang, X. Luo, L. Han, J. Huang, Z. Feng, Z. Chen, J. Xu, B. Peng and Z. L. Wang, *Nano Energy*, 2021, **81**, 105671.
- X. Li, B. Kang, F. Dong, F. Deng, L. Han, X. Gao, J. Xu, X. Hou, Z. Feng, Z. Chen, L. Liu and J. Huang, *Appl. Surf. Sci.*, 2022, **593**, 153422.
- N. Lu, M. Zhang, X. Jing, P. Zhang, Y. Zhu and Z. Zhang, *Energy Environ. Mater.*, 2022, DOI: [10.1002/eem2.12338](https://doi.org/10.1002/eem2.12338).
- N. Lu, X. Jing, J. Zhang, P. Zhang, Q. Qiao and Z. Zhang, *Chem. Eng. J.*, 2022, **431**, 134001.
- C. Y. Toe, J. Scott, R. Amal and Y. H. Ng, *J. Photochem. Photobiol., C*, 2019, **40**, 191–211.
- P. Dai, W. Li, J. Xie, Y. He, J. Thorne, G. McMahon, J. Zhan and D. Wang, *Angew. Chem., Int. Ed.*, 2014, **53**, 13493–13497.
- Y. Yang, D. Xu, Q. Wu and P. Diao, *Sci. Rep.*, 2016, **6**, 35158.
- C. Y. Toe, Z. Zheng, H. Wu, J. Scott, R. Amal and Y. H. Ng, *Angew. Chem., Int. Ed.*, 2018, **57**, 13613–13617.
- X. Deng, R. Li, S. Wu, L. Wang, J. Hu, J. Ma, W. Jiang, N. Zhang, X. Zheng, C. Gao, L. Wang, Q. Zhang, J. Zhu and Y. Xiong, *J. Am. Chem. Soc.*, 2019, **141**, 10924–10929.
- X. Wang, G. Chen and J. Zhang, *Catal. Commun.*, 2013, **31**, 57–61.
- L. Pan, J. H. Kim, M. T. Mayer, M.-K. Son, A. Ummadisingu, J. S. Lee, A. Hagfeldt, J. Luo and M. Grätzel, *Nat. Catal.*, 2018, **1**, 412–420.
- X. Jiang, J. Huang, Z. Bi, W. Ni, G. Gurzadyan, Y. Zhu and Z. Zhang, *Adv. Mater.*, 2022, **34**, e2109330.
- T. Wang, Y. Wei, X. Chang, C. Li, A. Li, S. Liu, J. Zhang and J. Gong, *Appl. Catal., B*, 2018, **226**, 31–37.
- Y. Wang, S. Cao, Y. Huan, T. Nie, Z. Ji, Z. Bai, X. Cheng, J. Xi and X. Yan, *Appl. Surf. Sci.*, 2020, **526**, 146700.
- M. E. Aguirre, R. Zhou, A. J. Eugene, M. I. Guzman and M. A. Grela, *Appl. Catal., B*, 2017, **217**, 485–493.
- J. Chen, S. Xie, L. Yue, F. Gong and Y. Zhang, *J. Mater. Sci.: Mater. Electron.*, 2021, **32**, 18900–18911.
- L. Jiang, N. Yang, C. Yang, X. Zhu, Y. Jiang, X. Shen, C. Li and Q. Sun, *Appl. Catal., B*, 2020, **269**, 118780.
- S. H. Mohamed, H. Zhao, H. Romanus, F. M. El-Hossary, M. Abo El-Kassem, M. A. Awad, M. Rabia and Y. Lei, *Mater. Sci. Semicond. Process.*, 2020, **105**, 104704.
- Y. Li and C. Zhao, *ACS Catal.*, 2017, **7**, 2535–2541.
- T. Zhang, P. Lin, N. Wei and D. Wang, *ACS Appl. Mater. Interfaces*, 2020, **12**, 20110–20118.
- T. Fujimura, W. Hikima, Y. Fukunaka and T. Homma, *Electrochem. Commun.*, 2019, **101**, 43–46.
- T. N. Chen, J. C. Kao, X. Y. Zhong, S. J. Chan, A. S. Patra, Y. C. Lo and M. H. Huang, *ACS Cent. Sci.*, 2020, **6**, 984–994.
- S. Zheng, L. Han, X. Luo, L. Sun, N. Li, Z. Zhang and X. Li, *Int. J. Energy Res.*, 2022, **46**, 4506–4515.
- C. Wang, Z. Li, J. Chen, Y. Yin and H. Wu, *Appl. Surf. Sci.*, 2018, **427**, 1092–1098.
- R. A. Zangmeister, T. A. Morris and M. J. Tarlov, *Langmuir*, 2013, **29**, 8619–8628.
- N. Li, L. Han, H. Zhang, J. Huang, X. Luo, X. Li, Y. Wang, W. Qian and Y. Yang, *Nano Res.*, 2022, 1–10, DOI: [10.1007/s12274-022-4588-8](https://doi.org/10.1007/s12274-022-4588-8).
- X. Li, Q. Liu, F. Deng, J. Huang, L. Han, C. He, Z. Chen, Y. Luo and Y. Zhu, *Appl. Catal., B*, 2022, **314**, 121502.
- X. Dong, Z. Fang, Y. Gu, X. Zhou and C. Tian, *Chin. Chem. Lett.*, 2022, DOI: [10.1016/j.ccl.2022.03.018](https://doi.org/10.1016/j.ccl.2022.03.018).
- P. P. Kunturu and J. Huskens, *ACS Appl. Energy Mater.*, 2019, **2**, 7850–7860.
- H. A. Lee, Y. Ma, F. Zhou, S. Hong and H. Lee, *Acc. Chem. Res.*, 2019, **52**, 704–713.
- R. N. Wenzel, *J. Phys. Colloid Chem.*, 1949, **53**, 1466–1467.
- R. N. Wenzel, *Ind. Eng. Chem.*, 1936, **28**, 988–994.
- T. Rajh, L. Chen, K. Lukas, T. Liu, M. Thurnauer and D. Tiede, *J. Phys. Chem. B*, 2002, **106**, 10543–10552.
- J. Moser, S. Punchedewa, P. P. Infelta and M. Graetzel, *Langmuir*, 1991, **7**, 3012–3018.
- C. Zhang, L. Gong, L. Xiang, Y. Du, W. Hu, H. Zeng and Z. K. Xu, *ACS Appl. Mater. Interfaces*, 2017, **9**, 30943–30950.

- 37 R. A. Zangmeister, T. A. Morris and M. Tarlov, *Langmuir*, 2013, **29**, 8619–8628.
- 38 H. Wu, Z. Zheng, C. Y. Toe, X. Wen, J. N. Hart, R. Amal and Y. H. Ng, *J. Mater. Chem. A*, 2020, **8**, 5638–5646.
- 39 J. Xiong, X. Li, J. Huang, X. Gao, Z. Chen, J. Liu, H. Li, B. Kang, W. Yao and Y. Zhu, *Appl. Catal., B*, 2020, **266**, 118602.
- 40 X. Ren, J. Shi, R. Duan, J. Di, C. Xue, X. Luo, Q. Liu, M. Xia, B. Lin and W. Tang, *Chin. Chem. Lett.*, 2022, **33**(10), 4700–4704.
- 41 H. Huang, B. Dai, W. Wang, C. Lu, J. Kou, Y. Ni, L. Wang and Z. Xu, *Nano Lett.*, 2017, **17**, 3803–3808.
- 42 B. He, C. Bie, X. Fei, B. Cheng, J. Yu, W. Ho, A. A. Al-Ghamdi and S. Wageh, *Appl. Catal., B*, 2021, **288**, 119994.
- 43 K. Das, S. N. Sharma, M. Kumar and S. De, *J. Phys. Chem. C*, 2009, **113**, 14783–14792.
- 44 W.-J. Ong, L. K. Putri, Y.-C. Tan, L.-L. Tan, N. Li, Y. H. Ng, X. Wen and S.-P. Chai, *Nano Res.*, 2017, **10**, 1673–1696.
- 45 P. An, W. Zhu, L. Qiao, S. Sun, Y. Xu, D. Jiang, M. Chen and S. Meng, *Dalton Trans.*, 2021, **50**, 2414–2425.
- 46 Y.-S. Chang, M. Choi, M. Baek, P.-Y. Hsieh, K. Yong and Y.-J. Hsu, *Appl. Catal., B*, 2018, **225**, 379–385.
- 47 H. Zhang, J. He, C. Zhai and M. Zhu, *Chin. Chem. Lett.*, 2019, **30**, 2338–2342.
- 48 W. Wang, X. Li, F. Deng, J. Liu, X. Gao, J. Huang, J. Xu, Z. Feng, Z. Chen and L. Han, *Chin. Chem. Lett.*, 2022, **33**(12), 5200–5207.
- 49 S. Zheng, S. Peng, Z. Wang, J. Huang, X. Luo, L. Han and X. Li, *Ceram. Int.*, 2021, **47**, 28304–28311.
- 50 F. Chen, W. Yu, Y. Qie, L. Zhao, H. Zhang and L.-H. Guo, *Chem. Eng. J.*, 2019, **373**, 58–67.
- 51 X. Jiang, Z. Zhang, M. Sun, W. Liu, J. Huang and H. Xu, *Appl. Catal., B*, 2021, **281**, 119473.
- 52 X. Song, Y. Li, Z. Wei, S. Ye and D. D. Dionysiou, *Chem. Eng. J.*, 2017, **314**, 443–452.
- 53 X. Zhou, B. Jin, J. Luo, X. Gu and S. Zhang, *J. Solid State Chem.*, 2017, **254**, 55–61.
- 54 L. D. M. Torquato, F. A. C. Pastrian, J. A. L. Perini, K. Irikura, A. P. de L. Batista, A. G. S. de Oliveira-Filho, S. I. Córdoba de Torresi and M. V. B. Zanoni, *Appl. Catal., B*, 2020, **261**, 118221.
- 55 F. Guo, J. Chen, J. Zhao, Z. Chen, D. Xia, Z. Zhan and Q. Wang, *Chem. Eng. J.*, 2020, **386**, 124014.
- 56 J. A. L. Perini, L. D. M. Torquato, K. Irikura and M. V. B. Zanoni, *J. CO2 Util.*, 2019, **34**, 596–605.
- 57 M. Li, S. Zhang, L. Li, J. Han, X. Zhu, Q. Ge and H. Wang, *ACS Sustainable Chem. Eng.*, 2020, **8**, 11465–11476.
- 58 X. Jie, N. Bao, B. Gong and S. Zhou, *Nano-Struct. Nano-Objects*, 2017, **12**, 98–105.